JOURNAL OF THERMOPHYSICS AND HEAT TRANSFER
Vol. 22, No. 2, April–June 2008

Numerical Computation of Radiative Heating Environment for Huygens Probe Entry Flight

Hiroshi Osawa*
Tohoku University, Sendai 980-8579, Japan
Shingo Matsuyama†
Japan Aerospace Exploration Agency, Chofu 182-8522, Japan
and
Naofumi Ohnishi,‡ Michiko Furudate,§ and Keisuke Sawada¶
Tohoku University, Sendai 980-8579, Japan

DOI: 10.2514/1.31654

A trajectory-based analysis for obtaining aerodynamic heating environment for the Huygens probe is carried out using the thermochemical nonequilibrium computational fluid dynamics code. Radiative heat transfer is accounted for in computational fluid dynamics calculations where a modern multiband radiation model is employed. In this study, we first compare the radiative heat flux obtained by the ray-tracing approach in three-dimensional space with that given by the tangent-slab approximation, to determine how the difference in obtaining radiative heat flux can alter the overall aerodynamic heating environment. We then explore the radiative cooling effect on surface heat flux through radiation coupled computational fluid dynamics calculations. It is shown that the radiative heat flux value at the stagnation point obtained by the ray-tracing approach becomes about 17–19% smaller than that given by the tangent-slab approximation due to body curvature at all the chosen trajectory points. Furthermore, it is also shown that the radiative cooling effect can reduce the surface radiative heat flux by almost the same amount at the stagnation point when computational fluid dynamics calculation coupled with radiation is conducted. It is therefore confirmed that, even for the relatively lower radiative heating rate such as for the Huygens entry flight, we need to employ the ray-tracing approach instead of the tangent-slab approximation, and also need to account for radiative cooling effect through radiation coupled computational fluid dynamics calculation, to evaluate the surface heating condition accurately.

Nomenclature

B_λ = Plank function at given wavelength λ, $W/(cm^2 \cdot sr \cdot \mu m)$
C_f = coefficient in Eq. (11) and Table 1, $m^3/(mol \cdot s)$
c = mass concentration
D = diffusion coefficient, m^2/s
$\tilde{D}$ = dissociation energy, J/kg
E_∞ = ionization potential, J/kg
e = total energy per unit volume, J/m^3
e_{el} = electronic energy per unit volume, J/m^3
e_v = vibrational energy per unit volume, J/m^3
e_v^* = vibrational energy per unit volume at the local T, J/m^3
$\mathbf{F}$ = x component of convective flux vector
$\mathbf{F}_v$ = x component of viscous flux vector
$\mathbf{G}$ = y component of convective flux vector
$\mathbf{G}_v$ = y component of viscous flux vector
$\mathbf{H}$ = source vector for axisymmetric flow
$\mathbf{H}_v$ = source vector for viscous flow
I_λ = radiative intensity at given wavelength λ, $W/(cm^2 \cdot sr \cdot \mu m)$
$I_{\lambda,n}$ = radiative intensity at given wavelength λ discretized in the direction of unit directional vector $\mathbf{\Omega}_n$, $W/(cm^2 \cdot sr \cdot \mu m)$
K_{eq} = equilibrium constant, 1 or mol/m^3
k_b = backward reaction rate coefficient, $m^3/(mol \cdot s)$ or $m^6/(mol^2 \cdot s)$
k_f = forward reaction rate coefficient, $m^3/(mol \cdot s)$
M = molecular weight, kg/mol
n = number density, cm^{-3}
$\mathbf{Q}$ = conservative variables
Q_{D-V} = vibrational energy change rate in dissociation, $J/(m^3 \cdot s)$
$Q_{E\text{imp}}$ = free electron energy change rate due to electron impact ionization, $J/(m^3 \cdot s)$
$Q_{E\text{Excit}}$ = electronic energy change rate due to chemical reactions, $J/(m^3 \cdot s)$
Q_{T-E} = free electron energy change rate for elastic collisions between electrons and heavy particles, $J/(m^3 \cdot s)$
Q_{T-V} = translational–rotational and vibrational–electronic energy exchange rate, $J/(m^3 \cdot s)$
q_{conv} = convective heat flux, W/m^2
q_{rad} = radiative heat flux, W/m^2
q_{vx} = vibrational–electronic heat conduction in direction x, W/m^2
q_{vy} = vibrational–electronic heat conduction in direction y, W/m^2
q_x = translational–rotational heat conduction in direction x, W/m^2

Presented as Paper 3772 at the 9th AIAA/ASME Joint Thermophysics and Heat Transfer Conference, San Francisco, CA, 5–8 June 2006; received 18 April 2007; revision received 20 December 2007; accepted for publication 26 December 2007.

*Graduate Student, Department of Aerospace Engineering. Student Member AIAA.
†Researcher, Computational Science Research Group, Institute of Aerospace Technology. Member AIAA.
‡Associate Professor, Department of Aerospace Engineering. Member AIAA.
§Assistant Professor, Department of Aerospace Engineering. Member AIAA.
¶Professor, Department of Aerospace Engineering. Associate Fellow AIAA.

q_y = translational–rotational heat conduction in direction y, W/m^2
R = universal gas constant, 8.314, J/(mol · K)
$\mathbf{S}$ = radiative source vector
Sc = Schmidt number
T = translational–rotational temperature, K
T_a = controlling temperature, K
T_{shock} = postshock translational–rotational temperature, K
T_v = vibrational–electronic temperature, K
$T_{v\text{shock}}$ = postshock vibrational–electronic temperature, K
T_w = wall surface temperature, K
u = x component of velocity, m/s
v = y component of velocity, m/s
$\mathbf{W}$ = source vector for thermochemistry
W_s = chemical source term for species s, kg/(m^3 · s)
W_v = vibrational–electronic energy source term, J/(m^3 · s)
w_n = weighting factor
α = constant in Eq. (14e)
ε = wall emissivity
η = constant for use in reaction rate coefficient in Eq. (11) and Table 1
θ_d = characteristic temperature of reaction in Eq. (11) and Table 1, K
κ = conductivity of translational–rotational temperature, W/(m · K)
κ_v = conductivity of vibrational–electronic temperature, W/(m · K)
κ_λ = absorption coefficient at given wavelength λ, cm^{-1}
λ = wavelength, μm
μ = viscosity of mixture, kg/(m · s)
ν = collision frequency, 1/s
ρ = total density, kg/m^3
$\tilde{\rho}_e$ = elemental density of element e, kg/m^3
ρ_s = density of species s, kg/m^3
σ = Stefan–Boltzmann constant, 5.67×10^{-8}, W/(m^2 · K^4)
σ_λ = absorption cross section at given wavelength λ, cm^2
τ_c = relaxation time for vibrational excitation given by the collision limits at high temperatures, s
τ_{ij} = shear stress tensor, N/m^2
τ_{LT} = relaxation time for vibrational excitation determined by the Landau–Teller equation using a Millikan–White formula, s
$\boldsymbol{\Omega}$ = solid angle, sr

Subscripts

e = elemental species e
s = species s
w = wall
λ = wavelength

I. Introduction

WHEN a space vehicle enters into the atmosphere of a planet, severe aerodynamic heating occurs. To protect the space vehicle from such aerodynamic heating, an appropriate thermal protection system (TPS) must be equipped. To design such a TPS, aerodynamic heating rates must be estimated accurately. Computational fluid dynamics (CFD) is indeed helpful in estimating the heating rates, although such estimation requires a sufficient understanding of physical phenomena that occur during the entry flight.

One of the most interesting planets/moons in the solar system is Saturn's largest moon Titan. Titan is known to have a dense atmosphere. Titan's atmosphere is composed mainly of nitrogen, a small amount of methane, and some argon. This is similar to the atmospheric composition of early Earth. Therefore, the European Space Agency (ESA) built the Huygens probe as a part of the joint National Aeronautics and Space Administration (NASA) and ESA mission to explore the Saturnian system named the Cassini-Huygens Mission. The Huygens probe entered into the atmosphere of Titan at a relative velocity of about 6.2 km/s and successfully landed on its surface on 14 January 2005.

Preflight predictions for the Huygens probe entry heating environment were made [1–3]. The entry velocity and postshock temperature during Titan atmospheric entry are relatively low compared to those for typical Earth entry. However, the radiative heating rates were predicted to be 2–3 times higher than the convective ones. This occurs because the methane dissociates in the shock layer and CN is formed. CN is known to be a strong radiator in both violet [B–X] and red [A–X] bands.

Recently, several studies to determine the Huygens probe aerodynamic heating environment have been revisited [4,5]. In these works, the radiative heating rates deduced from the results of the flowfield calculation are modified to account for the radiative cooling effect using an approximate technique developed by Tauber and Wakefield [6]. Moreover, the three-dimensional effects are accounted for by using the view-factor based approach [7]. In these CFD calculations, however, the flowfield is never altered due to the radiative cooling effect because radiation is totally uncoupled from the CFD calculation. During the entry flight, the temperature in the shock layer rises sufficiently high to emanate strong radiation. In such a strongly radiating flowfield, radiation can affect the flowfield properties. In turn, the flowfield can affect radiative properties. Therefore, to estimate the aerodynamic heating rates accurately, the flowfield must be calculated accounting for the coupling effect between flowfield and radiation. When radiation is strong, a radiative transfer from the stagnation region may raise the temperature in the downstream region. Therefore, multidimensional radiative transfer also needs to be accounted for.

In the ray-tracing approach for obtaining radiative heat flux, radiative intensity is first evaluated along each radiation ray by solving the radiative transfer equation. Radiative heat flux is then obtained by integrating radiative intensity over the solid angle. When the flowfield is optically thin, radiative intensity becomes anisotropic, that is, radiative intensity depends on the direction. Therefore, the accuracy of radiative heat flux depends on how radiative intensity is integrated over the solid angle. Anisotropy of radiative intensity can be accurately accounted for with an increased number of radiation rays. However, as the number of radiation rays is increased in the computational domain, the computing time is then increased substantially. To achieve a high accuracy of integration over the solid angle with a smaller number of radiation rays, we have employed the Gaussian quadrature method [8] in the present study.

The purpose of the present study is to obtain an aerodynamic heating environment for the Huygens probe along the entry trajectory. Radiation coupled calculation is carried out by assuming thermochemical nonequilibrium. Radiative heat flux is determined either using the ray-tracing approach in three-dimensional space or the tangent-slab approximation [9]. Comparison of these methods is made to clarify the possible influence over the obtained surface heating rate. Comparison is also made for radiation uncoupled and radiation coupled calculations to examine the radiative cooling effect in obtaining a surface heating rate.

II. Method of Calculation

A. Governing Equations

The governing equations are the Navier–Stokes equations in the axisymmetric form, which can be written as

$$\frac{\partial \mathbf{Q}}{\partial t} + \frac{\partial(\mathbf{F} - \mathbf{F}_v)}{\partial x} + \frac{\partial(\mathbf{G} - \mathbf{G}_v)}{\partial y} + \frac{\mathbf{H} - \mathbf{H}_v}{y} = \mathbf{W} + \mathbf{S} \qquad (1)$$

The components of the conservative variables, flux vectors, and source vectors are given, respectively, as follows:

$$\mathbf{Q}=\begin{bmatrix}\tilde{\rho}_e\\ \rho_s\\ \rho u\\ \rho v\\ e\\ e_v+e_{\mathrm{el}}\end{bmatrix},\qquad \mathbf{F}=\begin{bmatrix}\tilde{\rho}_e u\\ \rho_s u\\ \rho u^2+p\\ \rho uv\\ (e+p)u\\ (e_v+e_{\mathrm{el}})u\end{bmatrix}$$

$$\mathbf{G}=\begin{bmatrix}\tilde{\rho}_e v\\ \rho_s v\\ \rho uv\\ \rho v^2+p\\ (e+p)v\\ (e_v+e_{\mathrm{el}})v\end{bmatrix},\qquad \mathbf{W}=\begin{bmatrix}0\\ W_s\\ 0\\ 0\\ 0\\ W_v\end{bmatrix},\qquad \mathbf{S}=\begin{bmatrix}0\\ 0\\ 0\\ 0\\ -\nabla\cdot q_{\mathrm{rad}}\\ 0\end{bmatrix}$$

$$\mathbf{F}_v=\begin{bmatrix}-\tilde{\rho}_e u_e\\ -\rho_s u_s\\ \tau_{xx}\\ \tau_{xy}\\ \tau_{xx}u+\tau_{xy}v-q_x-q_{vx}-\sum_s \rho_s u_s h_s\\ -q_{vx}-\sum_s \rho_s e_{vs} u_s\end{bmatrix}$$

$$\mathbf{G}_v=\begin{bmatrix}-\tilde{\rho}_e v_e\\ -\rho_s v_s\\ \tau_{xy}\\ \tau_{yy}\\ \tau_{xy}u+\tau_{yy}v-q_y-q_{vy}-\sum_s \rho_s v_s h_s\\ -q_{vy}-\sum_s \rho_s e_{vs} v_s\end{bmatrix}$$

$$\mathbf{H}=\begin{bmatrix}\tilde{\rho}_e v\\ \rho_s v\\ \rho uv\\ \rho v^2\\ (e+p)v\\ (e_v+e_{\mathrm{el}})v\end{bmatrix}$$

$$\mathbf{H}_v=\begin{bmatrix}-\tilde{\rho}_e v_e\\ -\rho_s v_s\\ \tau_{xy}\\ \tau_{yy}-\tau_{\theta\theta}\\ \tau_{xy}u+\tau_{yy}v-q_y-q_{vy}-\sum_s \rho_s v_s h_s\\ -q_{vy}-\sum_s \rho_s e_{vs} v_s\end{bmatrix} \tag{2}$$

The shear stresses are assumed to be proportional to the first derivative of the mass averaged velocities and the Stokes assumption for the bulk viscosity is made. Therefore, the shear stresses are written as

$$\tau_{xx}=\frac{2}{3}\mu\left(2\frac{\partial u}{\partial x}-\frac{\partial v}{\partial y}-\frac{v}{y}\right) \tag{3a}$$

$$\tau_{xy}=\mu\left(\frac{\partial u}{\partial y}+\frac{\partial v}{\partial x}\right) \tag{3b}$$

$$\tau_{yy}=\frac{2}{3}\mu\left(2\frac{\partial v}{\partial y}-\frac{\partial u}{\partial x}-\frac{v}{y}\right) \tag{3c}$$

$$\tau_{\theta\theta}=\frac{2}{3}\mu\left(-\frac{\partial v}{\partial y}-\frac{\partial u}{\partial x}+2\frac{v}{y}\right) \tag{3d}$$

The heat conductions are given by the Fourier heat law

$$q_x=-\kappa\frac{\partial T}{\partial x},\qquad q_y=-\kappa\frac{\partial T}{\partial y} \tag{4a}$$

$$q_{vx}=-\kappa_v\frac{\partial T_v}{\partial x},\qquad q_{vy}=-\kappa_v\frac{\partial T_v}{\partial y} \tag{4b}$$

We consider the following 21 chemical species, N, N^+, N_2, N_2^+, C, C^+, C_2, CH, CH_2, CH_3, CH_4, H, H^+, H_2, CN, CN^+, NH, Ar, Ar^+, HCN, and e^-. In the present study, the concept of elemental species conservation is introduced [10]. The column vector of conservative variables thus becomes

$$\begin{aligned}\mathbf{Q}=(&\tilde{\rho}_{\mathrm{N}},\tilde{\rho}_{\mathrm{C}},\tilde{\rho}_{\mathrm{H}},\tilde{\rho}_{\mathrm{Ar}},\rho_{\mathrm{N}},\rho_{\mathrm{N}^+},\rho_{\mathrm{N}_2^+},\rho_{\mathrm{C}^+},\rho_{\mathrm{C}_2},\rho_{\mathrm{CH}},\rho_{\mathrm{CH}_2},\\ &\rho_{\mathrm{CH}_3},\rho_{\mathrm{CH}_4},\rho_{\mathrm{H}^+},\rho_{\mathrm{H}_2},\rho_{\mathrm{CN}},\rho_{\mathrm{CN}^+},\rho_{\mathrm{NH}},\rho_{\mathrm{Ar}^+},\rho_{\mathrm{HCN}},\rho u,\\ &\rho v,e,e_v+e_{\mathrm{el}})^t\end{aligned} \tag{5}$$

In the present study, charge neutrality is assumed and then ρ_{e^-} is omitted. Instead of solving the conservation equations for N_2, C, H, and Ar, the following relations are used to derive ρ_{N_2}, ρ_{C}, ρ_{H}, and ρ_{Ar}:

$$\begin{aligned}\frac{\tilde{\rho}_{\mathrm{N}}}{M_{\mathrm{N}}}=&\frac{\rho_{\mathrm{N}}}{M_{\mathrm{N}}}+\frac{\rho_{\mathrm{N}^+}}{M_{\mathrm{N}^+}}+2\frac{\rho_{\mathrm{N}_2}}{M_{\mathrm{N}_2}}+2\frac{\rho_{\mathrm{N}_2^+}}{M_{\mathrm{N}_2^+}}+\frac{\rho_{\mathrm{CN}}}{M_{\mathrm{CN}}}+\frac{\rho_{\mathrm{CN}^+}}{M_{\mathrm{CN}^+}}\\ &+\frac{\rho_{\mathrm{NH}}}{M_{\mathrm{NH}}}+\frac{\rho_{\mathrm{HCN}}}{M_{\mathrm{HCN}}}\end{aligned} \tag{6a}$$

$$\begin{aligned}\frac{\tilde{\rho}_{\mathrm{C}}}{M_{\mathrm{C}}}=&\frac{\rho_{\mathrm{C}}}{M_{\mathrm{C}}}+\frac{\rho_{\mathrm{C}^+}}{M_{\mathrm{C}^+}}+2\frac{\rho_{\mathrm{C}_2}}{M_{\mathrm{C}_2}}+\frac{\rho_{\mathrm{CH}}}{M_{\mathrm{CH}}}+\frac{\rho_{\mathrm{CH}_2}}{M_{\mathrm{CH}_2}}+\frac{\rho_{\mathrm{CH}_3}}{M_{\mathrm{CH}_3}}+\frac{\rho_{\mathrm{CH}_4}}{M_{\mathrm{CH}_4}}\\ &+\frac{\rho_{\mathrm{CN}}}{M_{\mathrm{CN}}}+\frac{\rho_{\mathrm{CN}^+}}{M_{\mathrm{CN}^+}}+\frac{\rho_{\mathrm{HCN}}}{M_{\mathrm{HCN}}}\end{aligned} \tag{6b}$$

$$\begin{aligned}\frac{\tilde{\rho}_{\mathrm{H}}}{M_{\mathrm{H}}}=&\frac{\rho_{\mathrm{CH}}}{M_{\mathrm{CH}}}+2\frac{\rho_{\mathrm{CH}_2}}{M_{\mathrm{CH}_2}}+3\frac{\rho_{\mathrm{CH}_3}}{M_{\mathrm{CH}_3}}+4\frac{\rho_{\mathrm{CH}_4}}{M_{\mathrm{CH}_4}}+\frac{\rho_{\mathrm{H}}}{M_{\mathrm{H}}}+\frac{\rho_{\mathrm{H}^+}}{M_{\mathrm{H}^+}}\\ &+2\frac{\rho_{\mathrm{H}_2}}{M_{\mathrm{H}_2}}+\frac{\rho_{\mathrm{NH}}}{M_{\mathrm{NH}}}+\frac{\rho_{\mathrm{HCN}}}{M_{\mathrm{HCN}}}\end{aligned} \tag{6c}$$

$$\frac{\tilde{\rho}_{\mathrm{Ar}}}{M_{\mathrm{Ar}}}=\frac{\rho_{\mathrm{Ar}}}{M_{\mathrm{Ar}}}+\frac{\rho_{\mathrm{Ar}^+}}{M_{\mathrm{Ar}^+}} \tag{6d}$$

The total density ρ is given by a sum of these elemental densities as

$$\rho=\sum_e \tilde{\rho}_e=\tilde{\rho}_{\mathrm{N}}+\tilde{\rho}_{\mathrm{C}}+\tilde{\rho}_{\mathrm{H}}+\tilde{\rho}_{\mathrm{Ar}} \tag{7}$$

The two-temperature model of Park is employed to describe the thermochemical nonequilibrium states [11]. The vibrational–electronic energy source term is given by a sum of five terms as

$$W_v=Q_{T-V}+Q_{T-E}+Q_{E\mathrm{imp}}+Q_{\mathrm{Excit}}+Q_{D-V} \tag{8}$$

Specifics of the respective terms will be given in Sec. II.C. The source vector for thermochemistry is modeled using reaction rates collected for the Titan atmospheric entry problem by Gökçen [12].

B. Transport Coefficients

The species viscosities for N, N^+, N_2, N_2^+, C, C^+, C_2, H, H^+, H_2, CN, CN^+, and HCN are given by a viscosity model for reacting flow developed by Blottner et al. [13]. The species viscosities of CH, CH_2, CH_3, CH_4, NH, Ar, and Ar^+ are deduced by the Lennard–Jones potential data taken from the Chemkin database [14]. The viscosity of e^- is obtained by using curve fits of [15]. The conductivities of translational–rotational temperature and vibrational–electronic temperature for each species are given by Eucken's relation [9]. Moreover, the total viscosity and conductivity of the gas are calculated using Wilke's semi-empirical mixing rule [16].

If we neglect the thermal diffusion effect and the pressure diffusion effect, the diffusion velocity of each component of the gas mixture is proportional to the gradient of the mass concentration. Therefore, the diffusive fluxes are written as

$$\rho_s u_s = -\rho D_s \frac{\partial c_s}{\partial x}, \qquad \rho_s v_s = -\rho D_s \frac{\partial c_s}{\partial y} \tag{9}$$

The diffusion coefficients are given by the total viscosity and the total density with a constant Schmidt number of 0.5 for all species, that is,

$$D_s = \frac{\mu}{Sc\rho} \tag{10}$$

C. Thermochemical Model

In the present calculation, 35 chemical reactions are considered as listed in Table 1 [12]. The forward reaction rate is obtained by

$$k_f(T_a) = C_f T_a^{\eta} \exp(-\theta_d/T_a) \tag{11}$$

where the parameters C_f, η, θ_d, and T_a are also listed in Table 1 [17–32]. The backward reaction rate is given by

$$k_b(T_a) = \frac{k_f(T_a)}{K_{\rm eq}(T_a)} \tag{12}$$

where $T_a = T$ for the dissociation and radical reactions (1–27), and $T_a = T_v$ for the ionization reactions (28–35). The equilibrium constants are calculated for these reactions at 2000, 4000, 6000, 8000, and 10,000 K. The resulting values are curve fitted by an expression

$$K_{\rm eq}(T_a) = \exp(A_1/Z + A_2 + A_3\,\ell_n(Z) + A_4 Z + A_5 Z^2) \tag{13}$$

where $Z = 10,000/T_a$. The parameters A_1–A_5 for the reactions are determined from the equilibrium compositions calculated by the NASA computer program Chemical Equilibrium with Applications (CEA) [33,34].

The vibrational–electronic energy source term in Eq. (8) can specifically be written as follows. The translational–rotational and vibrational–electronic energy exchange rate is given by the Landau–Teller equation modified by Park [35]

$$Q_{T-V} = \sum_{s=\text{molecule}} \rho_s \frac{e^*_{vs}(T) - e_{vs}}{\tau_{{\rm LT}s} + \tau_{cs}} \left| \frac{T_{\rm shock} - T_v}{T_{\rm shock} - T_{v\rm shock}} \right|^{S-1} \tag{14a}$$

where the relaxation time is obtained from a Millikan–White formula accounting for collision limits at high temperature [36]. The free electron energy change rate for elastic collisions between electrons and heavy particles is given by

$$Q_{T-E} = 3\rho_{e^-} R(T - T_v) \sum_{s \neq e^-} \frac{\nu_s}{M_s} \tag{14b}$$

The free electron energy loss due to electron impact ionization is given by

Table 1 Reaction rate coefficients [12] (M = possible collision partners)

	Reactions	C_f	η	θ_d	T_a	Source (Ref.)
	Dissociation reactions					
1.	$N_2 + M \leftrightarrow N + N + M$	7.00×10^{15}	−1.60	113,200	$\sqrt{TT_v}$	[17]
	enhanced rate for M = N, C, H	3.00×10^{16}	−1.60	113,200	$\sqrt{TT_v}$	
	enhanced rate for $M = e^-$	3.00×10^{18}	−1.60	113,200	T_v	
2.	$CH_4 + M \leftrightarrow CH_3 + H + M$	4.70×10^{41}	−8.20	59,200	$\sqrt{TT_v}$	[18]
3.	$CH_3 + M \leftrightarrow CH_2 + H + M$	1.02×10^{10}	0.00	45,600	$\sqrt{TT_v}$	[18]
4.	$CH_3 + M \leftrightarrow CH + H_2 + M$	5.00×10^{9}	0.00	42,800	$\sqrt{TT_v}$	[19]
5.	$CH_2 + M \leftrightarrow CH + H + M$	4.00×10^{9}	0.00	41,800	$\sqrt{TT_v}$	[19]
6.	$CH_2 + M \leftrightarrow C + H_2 + M$	1.30×10^{8}	0.00	29,700	$\sqrt{TT_v}$	[19]
7.	$CH + M \leftrightarrow C + H + M$	1.90×10^{8}	0.00	33,700	$\sqrt{TT_v}$	[19]
8.	$C_2 + M \leftrightarrow C + C + M$	1.50×10^{10}	0.00	71,600	$\sqrt{TT_v}$	[20]
9.	$H_2 + M \leftrightarrow H + H + M$	2.23×10^{8}	0.00	48,350	$\sqrt{TT_v}$	[18,21]
10.	$CN + M \leftrightarrow C + N + M$	2.53×10^{8}	0.00	71,000	$\sqrt{TT_v}$	[22,23]
11.	$NH + M \leftrightarrow N + H + M$	1.80×10^{8}	0.00	37,600	$\sqrt{TT_v}$	[24]
12.	$HCN + M \leftrightarrow CN + H + M$	3.57×10^{20}	−2.60	62,845	$\sqrt{TT_v}$	[25]
	Radical reactions					
13.	$CH_3 + N \leftrightarrow HCN + H + H$	7.00×10^{7}	0.00	0	T	[26]
14.	$CH_3 + H \leftrightarrow CH_2 + H_2$	6.03×10^{7}	0.00	7,600	T	[21]
15.	$CH_2 + N_2 \leftrightarrow HCN + NH$	4.82×10^{6}	0.00	18,000	T	[24]
16.	$CH_2 + N \leftrightarrow HCN + H$	5.00×10^{7}	0.00	0	T	[26]
17.	$CH_2 + H \leftrightarrow CH + H_2$	6.03×10^{6}	0.00	−900	T	[24]
18.	$CH + N_2 \leftrightarrow HCN + N$	4.40×10^{6}	0.00	11,060	T	[26]
19.	$CH + C \leftrightarrow C_2 + H$	2.00×10^{8}	0.00	0	T	[19]
20.	$C_2 + N_2 \leftrightarrow CN + CN$	1.50×10^{7}	0.00	21,000	T	[27]
21.	$CN + H_2 \leftrightarrow HCN + H$	2.95×10^{-1}	0.00	1,130	T	[28]
22.	$CN + C \leftrightarrow C_2 + N$	5.00×10^{7}	0.00	13,000	T	[17]
23.	$N + H_2 \leftrightarrow NH + H$	1.60×10^{8}	0.00	12,650	T	[29]
24.	$C + N_2 \leftrightarrow CN + N$	5.24×10^{7}	0.00	22,600	T	[18]
25.	$C + H_2 \leftrightarrow CH + H$	4.00×10^{8}	0.00	11,700	T	[30]
26.	$H + N_2 \leftrightarrow NH + N$	3.00×10^{6}	0.50	71,400	T	[31]
27.	$H + CH_4 \leftrightarrow CH_3 + H_2$	1.32×10^{-2}	3.00	4,045	T	[18,21]
	Ionization reactions					
28.	$N + N \leftrightarrow N_2^+ + e^-$	4.40×10^{1}	1.50	67,500	T_v	[17]
29.	$C + N \leftrightarrow CN^+ + e^-$	1.00×10^{9}	1.50	164,400	T_v	[32]
30.	$N + e^- \leftrightarrow N^+ + e^- + e^-$	2.50×10^{28}	−3.82	168,600	T_v	[17]
31.	$C + e^- \leftrightarrow C^+ + e^- + e^-$	3.70×10^{25}	−3.00	130,720	T_v	[17]
32.	$H + e^- \leftrightarrow H^+ + e^- + e^-$	2.20×10^{24}	−2.80	157,800	T_v	[17]
33.	$Ar + e^- \leftrightarrow Ar^+ + e^- + e^-$	2.50×10^{28}	−3.82	181,700	T_v	[32]
34.	$CN^+ + N \leftrightarrow CN + N^+$	9.80×10^{6}	0.00	40,700	T_v	[32]
35.	$C^+ + N_2 \leftrightarrow N_2^+ + C$	1.11×10^{8}	−0.11	50,000	T_v	[32]

$$Q_{E\text{imp}} = -\sum_{s=\text{N}^+,\text{C}^+,\text{H}^+,\text{Ar}^+} E_{\infty s} W_s \tag{14c}$$

The electronic energy change rate due to chemical reactions is given by

$$Q_{E\text{xcit}} = \sum_{s=\text{all}} e_{\text{el}s} W_s \tag{14d}$$

The vibrational energy loss or gain through dissociation or recombination reactions is set to be 30% of the corresponding dissociation energy, that is,

$$Q_{D-V} = -\sum_{s=\text{molecule}} \alpha \tilde{D}_s W_s \tag{14e}$$

where $\alpha = 0.3$ as suggested by Sharma [37].

D. Radiative Transfer

In the present study, radiative transfer is computed in a loosely coupled manner. The procedure of coupling calculation is as follows. First, flowfield calculation is carried out ignoring the radiative transfer effect. When the converged solution is obtained, the initial radiation field is calculated from the converged solution. Then, the flowfield is updated for a certain number of iterations while the radiation field is fixed. The radiation field is then updated using the new flowfield solution. This procedure is continued until both the flowfield and the radiation field are converged.

In the present study, the radiative transfer equation is solved using either the ray-tracing approach in three-dimensional space, or the tangent-slab approximation. A brief description of the former method is given in the next section. The absorption coefficients are calculated using the multiband radiation model. N_2, CN, N, C, and H are considered as contributors to radiation. In the present multiband radiation model, the absorption coefficients are evaluated at 10,000 wavelength points ranging from 750 to 15,000 Å, where we assume local thermodynamic equilibrium (LTE) with the vibrational–electronic temperature. The absorption coefficient of the gas mixture is expressed as a sum of those for individual species in the form of [38]

$$\kappa_\lambda = \sum_s n_s \sigma_\lambda^s \tag{15}$$

The cross section value is curve fitted using the five parameters of $A_{\lambda 1}^s$–$A_{\lambda 5}^s$ in the following form:

$$\sigma_\lambda^s = \exp\left[A_{\lambda 1}^s/z + A_{\lambda 2}^s + A_{\lambda 3}^s \ell_n(z) + A_{\lambda 4}^s z + A_{\lambda 5}^s z^2\right] \tag{16}$$

where $z = 10,000/T_v$.

E. Numerical Scheme

The governing equations are integrated by a cell-centered finite volume method. The Advection Upstream Splitting Method (AUSM-DV) scheme [39] is used to obtain the numerical convective flux. Second-order spatial accuracy is achieved by the Monotone Upstream-centered Scheme for Conservation Law (MUSCL) approach. The viscous flux is evaluated by central differencing. The time integration is performed by the lower–upper symmetric Gauss–Seidel (LU-SGS) method [40]. The Jacobian matrix corresponding to the source vector **W** is modified by introducing the idea of the diagonal implicit method of Eberhardt and Imlay [41]. The radiative source vector is added explicitly to the time integration.

The radiative transfer equation is given by

$$\mathbf{\Omega} \cdot \nabla I_\lambda = \kappa_\lambda (B_\lambda - I_\lambda) \tag{17}$$

The radiative heat flux is obtained by integrating the radiative intensity over the solid angle for 4π steradian

$$q_{\text{rad}} = \int_0^\infty \mathrm{d}\lambda \int_{4\pi} I_\lambda \mathbf{\Omega}\, \mathrm{d}\mathbf{\Omega} \tag{18}$$

The integration over the solid angle is evaluated by summing the contribution of radiative intensity in a specified direction multiplied by a differential solid angle. When three-dimensional radiative transfer is considered, the radiative source term in Eq. (1) is defined as a negative of the divergence of the radiative heat flux

$$-\nabla \cdot q_{\text{rad}} = -\int_0^\infty \mathrm{d}\lambda \int_{4\pi} \mathbf{\Omega} \cdot \nabla I_\lambda \, \mathrm{d}\mathbf{\Omega} \tag{19}$$

By substituting Eq. (17) into Eq. (19), we obtain

$$-\nabla \cdot q_{\text{rad}} = -\int_0^\infty \kappa_\lambda \left(4\pi B_\lambda - \int_{4\pi} I_\lambda \, \mathrm{d}\mathbf{\Omega}\right) \mathrm{d}\lambda \tag{20}$$

Here, the gas is not assumed to be optically thin, unlike in [7]; we retain the term of radiation absorption as it is. The integration over the solid angle is discretized by using the Gaussian quadrature method as

$$\int_{4\pi} I_\lambda \, \mathrm{d}\mathbf{\Omega} \cong \sum_n w_n I_{\lambda,n} \qquad [n = 1, 2, \ldots, N(N+2)] \tag{21}$$

where n is the index of the radiation rays which pass through nth Gaussian points. The total number of Gaussian points is $N(N+2)$ for the Nth order Gaussian quadrature method. We employ $N = 8$ with 80 radiation rays because this is the best value to compromise between the computational accuracy and the computational cost. A typical example of radiation rays emanating from a computational cell is shown in Fig. 1. Intensities are evaluated along the radiation rays in the three-dimensional mapping of the flowfield.

F. Boundary Condition

In the present study, the fully catalytic recombination processes of N and H atoms are considered. The recombination of all ions and electrons is also considered. The wall temperature is determined from the following radiative equilibrium condition with the wall emissivity of 0.9:

$$q_{\text{conv}} + q_{\text{rad}} = \varepsilon \sigma T_w^4 \tag{22}$$

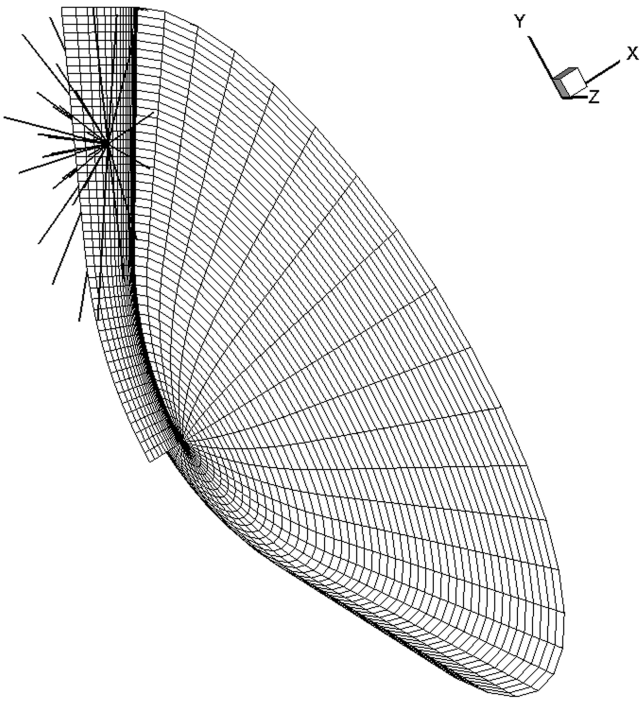

Fig. 1 Example of radiation rays emanating from a cell interface in three-dimensional space.

Table 2 Flow conditions at the trajectory points

Time, s	Velocity, m/s	Density, kg/m^3	Temperature, K
169	6048.8	3.64×10^{-5}	171.3
177	5886.3	7.20×10^{-5}	175.8
185	5489.6	1.83×10^{-4}	177.0
189	5126.3	2.96×10^{-4}	176.6
193	4705.2	3.79×10^{-4}	175.8
201	3660.4	7.43×10^{-4}	173.4

III. Flow Conditions

The Huygens heat shield has a 60-deg sphere–cone configuration with an open back face of 2.7-m diameter. The nose radius is 1.25 m. The freestream conditions at the chosen trajectory points are summarized in Table 2. The temperature and density at these trajectory points are obtained from the TitanGRAM code [42]. According to [43], the gas chromatograph mass spectrometer (GCMS) installed on the Huygens probe showed that Titan's atmosphere had only about 1.4% CH_4 and $\sim 4 \times 10^{-3}$% Ar. However, for the comparative purpose, the atmospheric composition employed in the present study is 97% N_2, 2.3% CH_4, and 0.7% Ar by volume, which was assumed in the previous Huygens entry flowfield predictions [4,5]. Figure 1 shows a typical example of computational mesh having 51×81 grid points used in the present study.

IV. Results and Discussion

A. Code Validation Study

The accuracy of the present multiband radiation model in obtaining the absorption coefficient is assessed by comparing the radiative heat flux distribution along the stagnation streamline with that given by the detailed line-by-line calculation [44]. The radiative heat fluxes are calculated for the flowfield at 189 s using the tangent-slab approximation. In Fig. 2, one can find that the wallward radiative heat flux distribution along the stagnation streamline agrees reasonably well for this case with a maximum difference in the heat flux value of 10%. This discrepancy is mainly caused by the inaccurate determination of the absorption cross section for the CN molecular band. In the present multiband radiation model, the absorption cross section obtained by the line-by-line calculation is first smoothed and then interpolated using Eq. (16) at the selected wavelength points. A typical example of such approximation is shown Fig. 3, where a comparison is made for the absorption coefficient computed by the multiband radiation model and that given by the line-by-line calculation ($n_{N_2} = 8.18 \times 10^{16}$ cm^{-3}, $n_{CN} = 5.19 \times 10^{14}$ cm^{-3}, $n_N = 8.00 \times 10^{15}$ cm^{-3}, $n_C = 1.49 \times 10^{15}$ cm^{-3}, $n_H = 7.97 \times 10^{15}$ cm^{-3}, and $T_v = 5280$ K). One can find that the absorption coefficient computed by the multiband radiation model agrees reasonably well with that given by the line-by-line calculation for the wavelength range from 750 to 4600 Å. However, the difference in the absorption coefficient becomes larger in the wavelength region longer than 4600 Å where the CN red band is dominant.

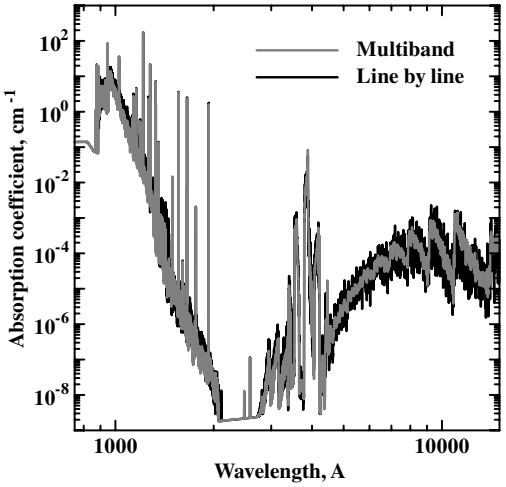

Fig. 3 Example of absorption coefficient ($n_{N_2} = 8.18 \times 10^{16}$ cm^{-3}, $n_{CN} = 5.19 \times 10^{14}$ cm^{-3}, $n_N = 8.00 \times 10^{15}$ cm^{-3}, $n_C = 1.49 \times 10^{15}$ cm^{-3}, $n_H = 7.97 \times 10^{15}$ cm^{-3}, and $T_v = 5280$ K).

Let us examine the convective heat flux at the stagnation point along the chosen trajectory points. The comparison of the obtained convective heat flux with that given by Wright et al. [5] for the Huygens entry flowfield is made for the radiation uncoupled case, because this is the only case available in [5]. As shown in Fig. 4, the computed convective heat flux value becomes consistently lower than that given by Wright et al., probably due to the differences in the transport properties (the species viscosity and the diffusion coefficients) and to the wall emissivity used in the calculation. The diffusion coefficients are assumed to be constant for all species in the present study, whereas the multicomponent diffusion model [45] is used in the study of Wright et al. The present radiative heat flux for the radiation coupled case is also compared with that given by Wright et al. [5]. In [5], the flowfield is obtained by using the LORE code [46] of the AOES Group, and the radiation field by the NEQAIR96 code [47] of NASA Ames Research Center. Note that the radiative heat flux in [5] is calculated by a postprocessing of the flowfield calculation without performing a coupled calculation, and modified by multiplying factors in order to include effects of the radiation

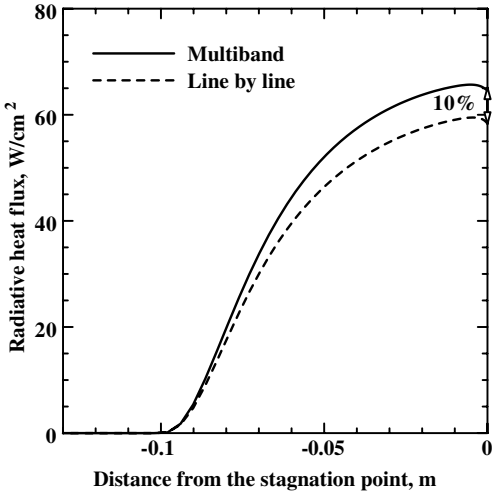

Fig. 2 Radiative heat flux distributions along the stagnation streamline at 189 s.

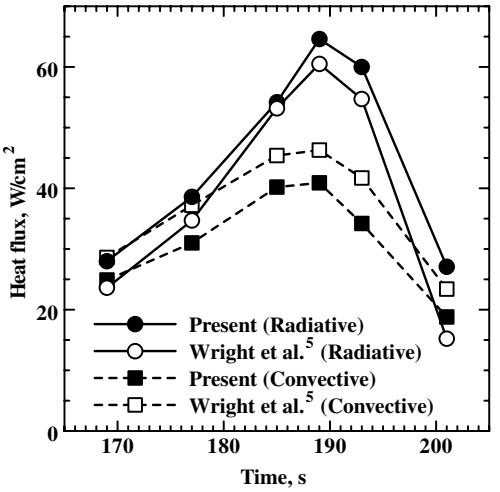

Fig. 4 Computed heat flux values at the stagnation point compared with the study of Wright et al. [5].

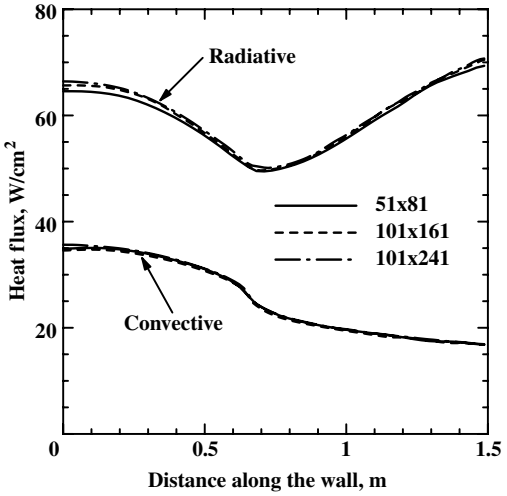

Fig. 5 Grid convergence of heat flux distribution along the body surface using the tangent-slab approximation at 189 s.

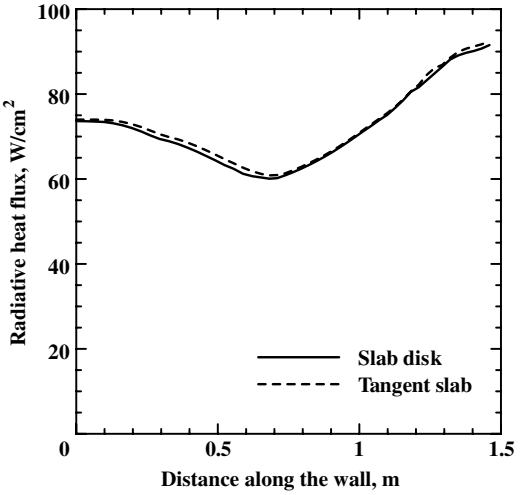

Fig. 6 Verification of the ray-tracing approach in three-dimensional space at 189 s.

cooling and the shock curvature. For comparative purposes, the correction for the shock curvature effect is canceled in Fig. 4 by dividing their original values by the factor of 0.75. It is found that the present radiative heat flux at the stagnation point agrees well with that given by Wright et al. except for the flowfield at 201 s, where the present radiative heat flux becomes higher. This difference can be attributed to the difference in the radiative heat flux value between the present multiband radiation model and the line-by-line calculation.

A grid convergence study is made by comparing the heat flux profiles for the flowfield at 189 s computed on the standard mesh (51×81 grid points) with those obtained on two finer meshes (101×161 and 101×241 grid points). The tangent-slab approximation is employed for obtaining the radiative heat fluxes. In Fig. 5, one can find that both the convective and radiative heat flux profiles computed on the standard mesh agree fairly well with those corresponding profiles computed on the fine meshes. These results justify the claim that the mesh convergence is safely attained for the results computed on the standard mesh.

B. Accuracy of Ray-Tracing Approach

In this section, the accuracy of the present ray-tracing approach for computing the radiative heat flux is examined. The flowfield properties along a certain line perpendicular to the wall are taken to set a slab layer (disk), in which physical quantities vary in the normal direction. The radius of the slab disk is set to be large enough to approximate an infinite slab disk. For such a slab disk, the tangent-slab approximation and the ray-tracing approach should yield the same radiative heat flux. In Fig. 6, the calculated radiative heat flux along the wall surface using radiation rays is compared with the result given by the tangent-slab approximation. The agreement is fairly good, indicating that the tangent-slab results can be reproduced by the ray-tracing approach. From this result, we can say that any difference found in the computed radiative heat flux value given by the ray-tracing approach and that given by the tangent-slab approximation is certainly due to the difference in approximation for obtaining radiative heat flux from the radiative intensity field.

C. Aerodynamic Heating for Huygens Probe with Radiative Heat Transfer

It is well known that the tangent-slab approximation can overestimate radiative heat flux at the stagnation point of a typical blunt body. It is therefore necessary to identify the amount of overestimated radiative heat flux by considering the ray-tracing approach in three-dimensional space in the radiation coupled calculation of the present entry flowfield. Hereafter, we denote the radiation coupled calculation using the ray-tracing approach in three-dimensional space as method A, the radiation coupled calculation using the tangent-slab approximation as method B, and the radiation uncoupled calculation as method C.

Figure 7 shows the temperature profiles along the stagnation streamline for the flowfield at 189 s. One can find that the computed shock standoff distance given by method A agrees well with that given by method B. Similarly, the translational–rotational temperature and vibrational–electronic temperature profiles agree well for these cases. On the other hand, the shock standoff distance given by method A is about 6% shorter and the temperatures behind the shock wave become slightly lower than those given by method C, respectively.

The mole fraction distributions of N_2, CH_4, CN, N, C, and H computed by method A along the stagnation streamline for the flowfield at 189 s are shown in Fig. 8. The mole fraction distributions computed by method B agree well with those given by method A and are not shown here. In Fig. 8, a rapid dissociation of CH_4 occurs behind the shock wave. N_2 is also dissociated behind the shock wave and the mole fraction is decreased by about 10% in the shock layer. However, N_2 is still the dominant species in the shock layer. These dissociation reactions result in the production of N and H atoms, whose mole fractions reach to 10%, respectively. The mole fraction of CN which is the main contributor to radiation becomes about 1.8% at the shock wave and is then decreased gradually toward the wall, but is suddenly increased again in the boundary layer due to the catalytic recombination process.

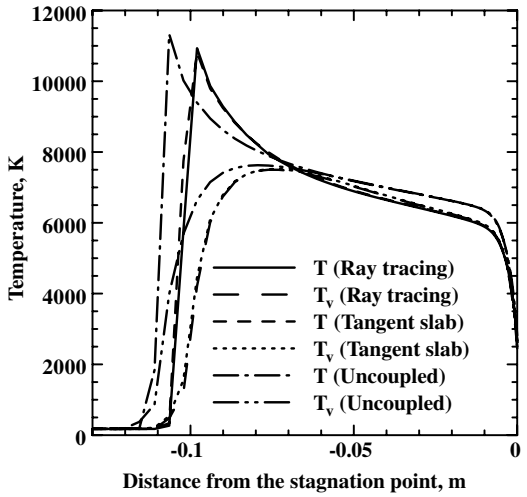

Fig. 7 Temperature distributions along the stagnation streamline computed by methods A, B, and C at 189 s.

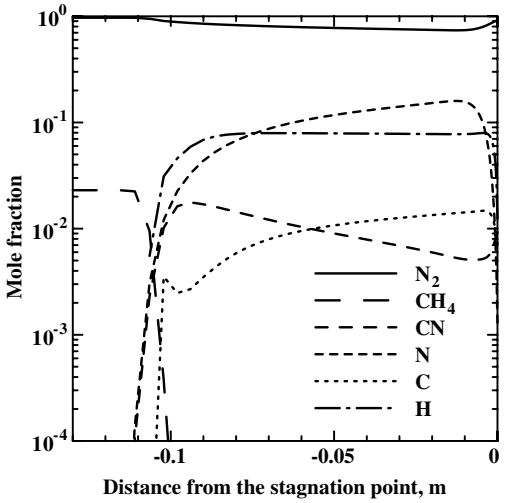

Fig. 8 Mole fraction distributions along the stagnation streamline computed by method A at 189 s.

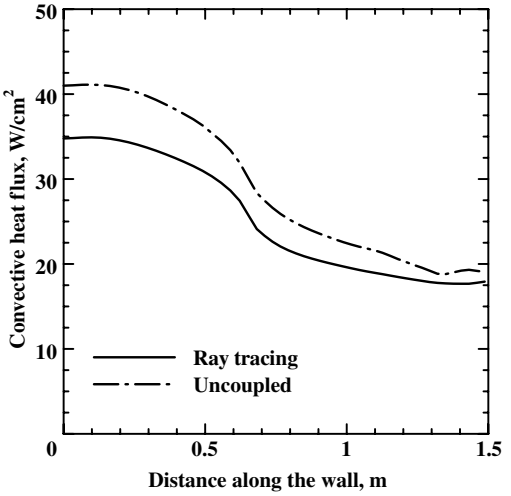

Fig. 10 Convective heat flux distributions along the body surface computed by methods A and C at 189 s.

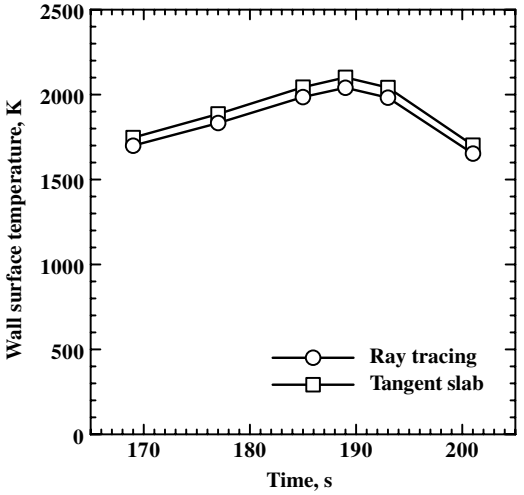

Fig. 9 Wall surface temperatures at the stagnation point computed by methods A and B.

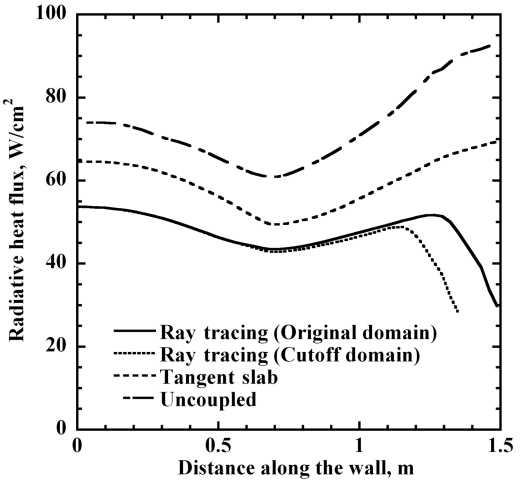

Fig. 11 Radiative heat flux distributions along the body surface computed by methods A, B, and C at 189 s.

The radiative equilibrium wall surface temperatures at the stagnation point computed by methods A and B are shown in Fig. 9. The wall surface temperature computed by method A becomes about 3% lower than those given by method B at all the trajectory points. The maximum temperature value of 2040 K is obtained by method A, whereas 2100 K is obtained by method B for the flowfield at 189 s.

The convective heat fluxes along the body surface for the flowfield at 189 s obtained by methods A and C are shown in Fig. 10. The computed convective heat flux given by method B agrees fairly well with that given by method A over the entire surface at all the trajectory points and hence is not shown here. It is indicated that, when radiation is coupled with the flowfield, the convective heat flux is decreased over the entire surface. Figure 11 shows radiative heat fluxes along the body surface for the flowfield at 189 s computed by methods A, B, and C. One finds that method A gives consistently lower radiative heat flux over the entire surface than that given by method B. In particular, the radiative heat flux at around the stagnation region given by method A becomes about 17% lower than that given by method B. This is because the shock layer near the stagnation point has a smaller radius of curvature. On the other hand, the radiative heat flux at around the midcone region given by method A is lower than that of method B by 12%. The shape of the shock wave at around the midcone region is almost conical where the tangent-slab approximation can give a better agreement than in the stagnation region. Note that the radiative heat flux at the stagnation point given by method B is about 13% lower than that given by method C. This amount is comparable to the difference between those given by methods A and B. For the other five trajectory points, similar tendencies are obtained in the convective and the radiative heat flux distributions. The radiative heat fluxes at around the stagnation and midcone regions given by method A become, respectively, about 17–19% and 10–12% lower than those given by method B. These results clearly indicate that not only the ray-tracing approach in the three-dimensional space but also the coupling between flowfield and radiation is certainly needed to predict the radiative heating rate accurately.

In Fig. 11, we can find that the radiative heat flux first decreases from the stagnation point up to the midcone region, as in the case of convective heat flux, and then it increases toward the downstream region because the number density of CN substantially increases and enhances radiative heat flux at that region. Furthermore, the radiative heat flux given by method A suddenly decreases at the downstream edge as shown in Fig. 11 whereas it does not occur in the result given by method B. This is because the radiation incoming from the flowfield outside of the computational domain, where no flowfield properties are available, is assumed to be zero in method A. If we cut off the computational domain at a certain position in the upper stream, the turning point in the radiative heat flux profile moves toward the upper stream accordingly, as shown in Fig. 11. This result shows that the influence of the boundary condition on the estimation of the radiative heat flux is limited to the region within 0.25 m

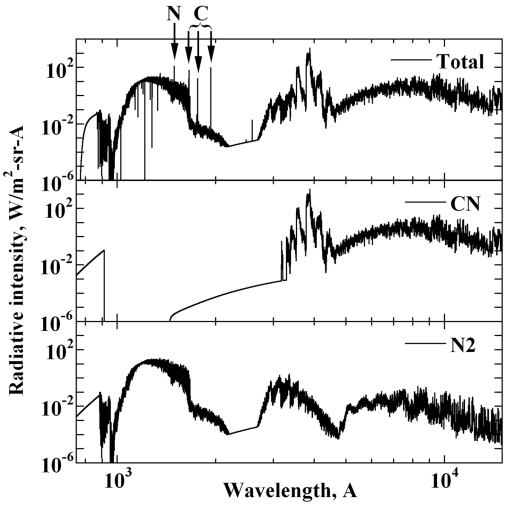

Fig. 12 Typical example of total radiative intensities and radiative intensities considering only CN or only N_2.

upstream from the exit-flow boundary of the computational domain in the present calculation.

Figure 12 shows a typical example of total radiative intensities considering five species as radiative species at the stagnation point. Major atomic lines are indicated in this figure. Radiative intensities considering only CN or only N_2 are also displayed in Fig. 12. It is found that CN has the strongest intensities among the five species we considered. When calculated from the CN radiative intensities, the amount of radiative heat flux accounts for 95% of the total radiative heat flux.

Finally, in Fig. 13, we compare the total heat flux at the stagnation point computed by methods A and B at each trajectory point. One can find that method A gives the maximum total heat flux of 88.5 W/cm^2, while method B gives the value of 99.5 W/cm^2 at the peak heating point. The fraction of radiative heating becomes about 60% of the total heat flux computed by method A, while the fraction of radiative heating becomes about 65% given by method B at the peak heating point.

V. Conclusions

A trajectory-based analysis for obtaining an aerodynamic heating environment for the Huygens probe is carried out using the thermochemical nonequilibrium CFD code that is loosely coupled with radiative heat transfer calculation. A multiband radiation model having 10,000 wavelength points is employed in the radiation calculation. The radiative heat flux values computed by radiation coupled calculation using the tangent-slab approximation are found to agree well with those given by Wright et al. It is shown that the radiative heat flux value at the stagnation point obtained by the ray-tracing approach becomes about 17–19% smaller than that given by the tangent-slab approximation due to body curvature at all the chosen trajectory points. Furthermore, it is also shown that the radiative cooling effect can reduce the surface radiative heat flux by almost the same amount at the stagnation point when a radiation coupled CFD calculation is made. It is therefore concluded that both the ray-tracing approach for obtaining radiative heat flux and the radiation coupled calculation to account for a radiative cooling effect are essentially important for evaluating the surface heating rate accurately for the Huygens entry flight.

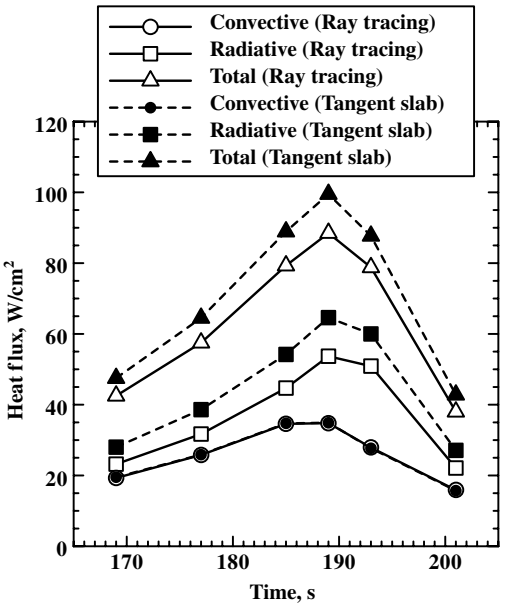

Fig. 13 Heat fluxes at the stagnation point computed by methods A and B.

Acknowledgments

The authors would like to express their appreciation to Yousuke Ogino, Department of Aerospace Engineering, Tohoku University, for providing the computer codes to carry out the ray-tracing radiation calculations in advance of publications. The authors also would like to thank Kenichi Sugai, Department of Aerospace Engineering, Tohoku University, for helping us to smoothly perform the radiation calculation for the present cases.

References

[1] Baillion, M., Pallegoix, J. F., and Soler, J., "Huygens Probe Aerothermodynamics," AIAA Paper 97–2476, June 1997.

[2] Baillion, M., Taquin, G., and Soler, J., "Huygens Probe Radiative Environment," *Proceedings of the 19th International Symposium on Shock Waves*, Springer–Verlag, New York, 1993, pp. 339–346.

[3] Baillion, M., and Taquin, G., "Radiative Heat Flux: Theoretical and Experimental Predictions for Titan Entry Probe," Capsule Aerothermodynamics, AGARD, Rept. 808, May 1997.

[4] Hollis, B. R., Striepe, S. A., Wright, M. J., Bose, D., Sutton, K., and Takashima, N., "Prediction of the Aerothermodynamic Environment of the Huygens Probe," AIAA Paper 2005–4816, June 2005.

[5] Wright, M. J., Olejniczak, J., Walpot, L., Raynaud, E., Magin, T., Caillaut, L., and Hollis, B. R., "A Code Calibration Study for Huygens Entry Aeroheating," AIAA Paper 2006-0382, Jan. 2006.

[6] Tauber, M. E., and Wakefield, R. M., "Heating Environment and Protection During Jupiter Entry," *Journal of Spacecraft and Rockets*, Vol. 8, No. 6, 1971, pp. 630–636.

[7] Bose, D., and Wright, M. J., "View-Factor Based Radiation Transport in a Hypersonic Shock Layer," *Journal of Thermophysics and Heat Transfer*, Vol. 18, No. 4, 2004, pp. 553–555.

[8] Modest, M. F., *Radiative Heat Transfer*, Academic Press, New York, 1993, pp. 498–538.

[9] Vincenti, W. G., and Kruger, C. H., *Introduction of Physical Gas Dynamics*, Wiley, New York, 1967, pp. 375–522.

[10] Hassan, B., Candler, G. V., and Olynick, D. R., "Thermo-Chemical Nonequilibrium Effects on the Aerothermodynamics of Aerobraking Vehicles," *Journal of Spacecraft and Rockets*, Vol. 30, No. 6, 1993, pp. 647–655.

[11] Park, C., "Assessment of Two-Temperature Kinetic Model for Ionizing Air," *Journal of Thermophysics and Heat Transfer*, Vol. 3, No. 3, 1989, pp. 233–244.

[12] Gökçen, T., "N_2-CH_4-Ar Chemical Kinetic Model for Simulations of Titan Atmospheric Entry," *Journal of Thermophysics and Heat Transfer*, Vol. 21, No. 1, 2007, pp. 9–18. doi:10.2514/1.22095

[13] Blottner, F. G., Johnson, M., and Ellis, M., "Chemically Reacting Viscous Flow Program for Multi-Component Gas Mixture," Sandia National Laboratories, Rept. SC-RR-70-754, 1971.

[14] Kee, R. J., Dixon-Lewis, G., Warnatz, J., Coltrin, M. E., and Miller, J. A., "A Fortran Computer Code Package for the Evaluation of Gas-Phase, Multicomponent Transport Properties," Sandia National Laboratories, Rept. SAND86-8246, 1986.

[15] Ahn, H.-K., Sawada, K., and Park, C., "CFD Calculation of Heat Fluxes in Turbulent Flow for Pioneer-Venus Probes," AIAA Paper 98-0833, Jan. 1998.

[16] Wilke, C. R., "A Viscosity Equation for Gas Mixtures," *Journal of Chemical Physics*, Vol. 18, No. 4, 1950, pp. 517–519. doi:10.1063/1.1747673

[17] Park, C., Jaffe, R. L., and Partridge, H., "Chemical-Kinetic Parameters of Hyperbolic Earth Entry," *Journal of Thermophysics and Heat Transfer*, Vol. 15, No. 1, 2001, pp. 76–90.

[18] Baulch, D. L., Cobos, C. J., Cox, R. A., Frank, P., Hayman, G., Just, T., Kerr, J. A., Murrells, T., Pilling, M. J., Troe, J., Walker, R. W., and Warnatz, J., "Evaluated Kinetic Data for Combustion Modelling. Supplement 1," *Journal of Physical and Chemical Reference Data*, Vol. 23, No. 6, 1994, pp. 847–1033.

[19] Dean, A. J., and Hanson, R. K., "CH and C-Atom Time Histories in Dilute Hydrocarbon Pyrolysis: Measurements and Kinetics Calculations," *International Journal of Chemical Kinetics*, Vol. 24, No. 6, 1992, pp. 517–532. doi:10.1002/kin.550240602

[20] Kruse, T., and Roth, P., "Kinetics of C_2 Reactions During High-Temperature Pyrolysis of Acetylene," *Journal of Physical Chemistry A*, Vol. 101, No. 11, 1997, pp. 2138–2146. doi:10.1021/jp963373o

[21] Baulch, D. L., Cobos, C. J., Cox, R. A., Esser, C., Frank, P., Just, T., Kerr, J. A., Pilling, M. J., Troe, J., Walker, R. W., and Warnatz, J., "Evaluated Kinetic Data for Combustion Modelling," *Journal of Physical and Chemical Reference Data*, Vol. 21, No. 3, 1992, pp. 411–734.

[22] Park, C., Howe, J. T., Jaffe, R. L., and Candler, G. V., "Review of Chemical-Kinetic Problems of Future NASA Missions, 2: Mars Entries," *Journal of Thermophysics and Heat Transfer*, Vol. 8, No. 1, 1994, pp. 9–23.

[23] Tsang, W., "Chemical Kinetic Data Base for Propellant Combustion 2: Reactions Involving CN, NCO, and HNCO," *Journal of Physical and Chemical Reference Data*, Vol. 21, No. 4, 1992, pp. 753–791.

[24] NIST Chemical Kinetic Database, Ver. 7.0, http://kinetics.nist.gov/kinetics/index.jsp, 2003 [retrieved 14 Feb. 2008].

[25] Tsang, W., and Herron, J. T., "Chemical Kinetic Data Base for Propellant Combustion 1. Reactions Involving NO, NO_2, HNO, HNO_2, HCN, and N_2O," *Journal of Physical and Chemical Reference Data*, Vol. 20, No. 4, 1991, pp. 609–663.

[26] Dean, A. J., Hanson, R. K., and Bowman, C. T., "High Temperature Shock Tube Study of Reactions of CH and C-Atoms with N_2," *Twenty-Third Symposium (International) on Combustion*, The Combustion Institute, Pittsburgh, PA, 1990, pp. 259–265.

[27] Sommer, T., Kruse, T., Roth, P., and Hippler, H., "Perturbation Study on the Reaction of C_2 with N_2 in High-Temperature $C_{60}/Ar + N_2$ Mixtures," *Journal of Physical Chemistry A*, Vol. 101, No. 20, 1997, pp. 3720–3725. doi:10.1021/jp962779y

[28] Wooldridge, S. T., Hanson, R. K., and Bowman, C. T., "A Shock Tube Study of Reactions of CN with HCN, OH, and H_2 Using CN and OH Laser Absorption," *International Journal of Chemical Kinetics*, Vol. 28, No. 4, 1996, pp. 245–258. doi:10.1002/(SICI)1097-4601(1996)28:4<245::AID-KIN2>3.0.CO;2-V

[29] Davidson, D. F., and Hanson, R. K., "High Temperature Reaction Rate Coefficients Derived from N-Atom ARAS Measurements and Excimer Photolysis of NO," *International Journal of Chemical Kinetics*, Vol. 22, No. 8, 1990, pp. 843–861. doi:10.1002/kin.550220805

[30] Dean, A. J., Davidson, D. F., and Hanson, R. K., "A Shock Tube Study of Reactions of C Atoms with H_2 and O_2 Using Excimer Photolysis of C_3O_2 and C Atom Atomic Resonance Absorption Spectroscopy," *Journal of Physical Chemistry*, Vol. 95, No. 1, 1991, pp. 183–191. doi:10.1021/j100154a037

[31] Roose, T. R., Hanson, R. K., and Kruger, C. H., "Decomposition of NO in the Presence of NH_3," *Proceedings of the 11th International Symposium on Shock Tubes and Waves*, University of Washington Press, Seattle, WA, 1977, pp. 245–253.

[32] Nelson, H. F., Park, C., and Whiting, E. E., "Titan Atmospheric Composition by Hypervelocity Shock-Layer Analysis," *Journal of Thermophysics and Heat Transfer*, Vol. 5, No. 2, 1991, pp. 157–165.

[33] Gordon, S., and McBride, B. J., "Computer Program for Calculation of Complex Chemical Equilibrium Compositions and Applications," NASA RP-1311, Oct. 1994.

[34] The NASA Computer Program CEA (Chemical Equilibrium with Applications) http://www.grc.nasa.gov/WWW/CEAWeb, Oct. 2003 [retrieved 14 Feb. 2008].

[35] Park, C., *Nonequilibrium Hypersonic Aerothermodynamics*, Wiley, New York, 1989, pp. 124–129.

[36] Millikan, R. C., and White, D. R., "Systematics of Vibrational Relaxation," *Journal of Chemical Physics*, Vol. 39, No. 12, 1963, pp. 3209–3213. doi:10.1063/1.1734182

[37] Sharma, S. P., Huo, W. M., and Park, C., "Rate Parameters for Coupled Vibration-Dissociation in a Generalized SSH Approximation," *Journal of Thermophysics and Heat Transfer*, Vol. 6, No. 1, 1992, pp. 9–21.

[38] Park, C., and Milos, F. S., "Computational Equations for Radiating and Ablating Shock Layers," AIAA Paper 90-0356, Jan. 1990.

[39] Wada, Y., and Liou, M. S., "A Flux Splitting Scheme with High-Resolution and Robustness for Discontinuities," AIAA Paper 94-0083, Jan. 1994.

[40] Yoon, S., and Jameson, A., "Lower-Upper Symmetric-Gauss-Seidel Method for the Euler and Navier-Stokes Equations," *AIAA Journal*, Vol. 26, No. 9, 1988, pp. 1025–1026.

[41] Eberhardt, S., and Imlay, S., "Diagonal Implicit Scheme for Computing Flows with Finite Rate Chemistry," *Journal of Thermophysics and Heat Transfer*, Vol. 6, No. 2, 1992, pp. 208–216.

[42] Justus, C. G., Duvall, A., and Johnson, D. L., "Engineering-Level Model Atmospheres for Titan and Neptune," AIAA Paper 2003-4803, July 2003.

[43] Niemann, H. B., Atreya, S. K., Bauer, S. J., Carignan, G. R., Demick, J. E., Frost, R. L., Gautier, D., Haberman, J. A., Harpold, D. N., Hunten, D. M., Israel, G., Lunine, J. I., Kasprzak, W. T., Owen, T. C., Paulkovich, M., Raulin, F., Raaen, E., and Way, S. H., "The Abundances of Constituents of Titan's Atmosphere from the GCMS Instrument on the Huygens Probe," *Nature (London)*, Vol. 438, No. 7069, 2005, pp. 779–784. doi:10.1038/nature04122

[44] Arnold, J. O., Cooper, D. M., Park, C., and Prakash, S. G., "Line-by-Line Transport Calculations for Jupiter Entry Probes," *Entry Heating and Thermal Protection*, edited by W. B. Olstad, Vol. 69, Progress in Astronautics and Aeronautics, AIAA, New York, 1980, pp. 52–82; also AIAA Paper 79-1082, June 1979.

[45] Sutton, K., and Gnoffo, P. A., "Multi-Component Diffusion with Application to Computational Aerothermodynamics," AIAA Paper 98-2575, June 1998.

[46] Walpot, L., "Development and Application of a Hypersonic Flow Solver," Ph.D. Thesis, Delft University of Technology, The Netherlands, May 2002.

[47] Whiting, E. E., Park, C., Yen, L., Arnold, J. O., and Paterson, J. A., "NEQAIR96, Nonequilibrium and Equilibrium Radiative Transport and Spectra Program User's Manual," NASA RP-1389, Dec. 1996.